PCCP

PAPER

View Article Online
View Journal | View Issue

Cite this: *Phys. Chem. Chem. Phys.*, 2017, **19**, 10453

Anisotropic transport in 1T′ monolayer MoS_2 and its metal interfaces

Dipankar Saha * and Santanu Mahapatra

Received 7th February 2017,
Accepted 24th March 2017

DOI: 10.1039/c7cp00816c

rsc.li/pccp

The investigation of crystallographic orientation dependent carrier transport in a material could lead to novel electronic devices and circuit applications. Although the out-of-plane carrier transport in layered transition metal dichalcogenides (TMDs) is expected to differ from its normal counterpart, in-plane anisotropy is not so common in such materials. The symmetric honeycomb structure of a semiconducting 2H phase MoS_2 crystal limits the in-plane anisotropy. However such possibility in a distorted 1T phase *i.e.*, the 1T′ phase of the MoS_2 crystal has not yet been explored. Using first principles based quantum transport calculations we demonstrate that, due to the clusterization of "Mo" atoms in 1T′ MoS_2, the transmission along the zigzag direction is significantly higher than that in the armchair direction. Since the metallic 1T′ phase finds application in realizing low resistive metal–MoS_2 contacts, we further extend this study to the 1T′ MoS_2 interface with gold and palladium by developing atomistic models for the optimized metal–1T′ MoS_2 edge contact geometries. Analysing the transmission spectra and electronic conductance values we show that the metal–zigzag 1T′ MoS_2 interfaces provide best case results, irrespective of the choice of metal. Moreover, we observe that edge contact geometries with the gold electrodes offer lesser resistances, compared to those with palladium electrodes. Our findings could pave the way for designing high performance phase-engineered MoS_2 based electron devices.

1 Introduction

Atomically thin layered transition metal dichalcogenides (TMDs), being all-surface in nature, can exhibit unique electronic, optical and mechanical properties.[1–5] Amongst the others, semiconducting molybdenum disulfide (2H phase MoS_2) is considered to be the most promising one, owing to its abundance in nature, near-silicon band gap, increased photo luminescence and higher mechanical flexibility.[2,3,5,6] Strong light–matter interaction as well as tunable direct band gap make this two dimensional material an ideal choice for optoelectronic devices *e.g.* photo-detectors, photovoltaics, *etc.*[7–9] In addition to that, as the replacement for conventional silicon (Si)-based channel materials for sub-decananometer FETs (field effect transistors), investigation of monolayer MoS_2 has become enormously popular over the past few years.[10–14] Atomic layer semiconducting MoS_2 channels have the edge over silicon thin films, owing to properties like the absence of dangling bonds at the surface, excellent on/off current ratio, *etc.*[10] However, the success of these atomically thin TMDs in replacing the conventional Si-based technology greatly depends on how we deal with the issues *e.g.*, forming low resistance source/drain contacts, achieving higher effective mobility, ensuring large-scale controlled growth, *etc.*[13,15–18]

Of late experimental evidence demonstrates the coexistence of metallic and semiconducting phases of MoS_2 in the same crystal plane.[13,19–21] Such in-plane hetero-phase MoS_2 structures could be useful, owing to their metallic extension parts which can achieve excellent impedance matching with various metal contacts.[13] In such hetero-phase MoS_2 flakes, the in-plane junctions formed at phase boundaries mainly dictate the carrier transport. In order to further access the electronic-structures of those interfaces, we find a few recent nonequilibrium Green's function (NEGF)-density functional theory (DFT) studies,[22,23] where the atomistic models of geometry optimized in-plane metallic–semiconducting and/or metallic–semiconducting–metallic hetero-phase MoS_2 structures have been delineated in great detail. However, a comprehensive study on the transparency of metal–1T′ MoS_2 interfaces to charge carrier transport is still due.

The details of relative energetic stability of various phases (2H, 1T and 1T′) of MoS_2 have already been reported in the literature.[22,24–26] Taking the presence of imaginary or negative frequencies into consideration, we find that the metallic 1T phase of MoS_2 is dynamically unstable.[22,25] However, redefining its lattice vectors, the 1T crystal may further relax its energy to form a distorted 1T or 1T′ phase which is thermodynamically more stable.[22,24] In this work, we emphasize on the orientation dependent anisotropic transport in single layer 1T′ MoS_2. For ReS_2 (a group 7 TMD), the details of atomic orientation dependent anisotropic transport properties have been demonstrated in ref. 27.

Nano-Scale Device Research Laboratory, Department of Electronic Systems Engineering, Indian Institute of Science(IISc) Bangalore, Bangalore-560012, India. E-mail: dipsah_etc@yahoo.co.in, santanu@dese.iisc.ernet.in

Using an annular dark field (ADF) image of an exfoliated monolayer, Lin *et al.* have shown the arrangement of diamond shaped chains (formed by "Re" atoms) and found an angle of $\sim 119.8^{\circ}$ between the [100] and [010] axes. Further, they have observed that the two terminal conductance parallel to the diamond shaped chains (along the [010] axis) is an order of magnitude larger than that in the perpendicular direction.[27] However, for the semiconducting phase MoS_2 (a group 6 TMD, with a trigonal prismatic structure), such orientation dependency of the carrier transport is generally not expected. Although, for monolayer 2H phase MoS_2, the effective mass of electrons is almost isotropic, a recent theoretical study[28] demonstrated that the orientation in the armchair or zigzag direction can play a role in carrier transport at the ballistic limit. From the calculated transfer characteristics of MoS_2 field effect transistors, Liu *et al.* further predicted that the drain current values in the zigzag direction remain always larger than those in the armchair direction.[28] Such observations motivated us to investigate the anisotropic transport in other phases of monolayer MoS_2.

Anisotropic carrier transport in a material can lead to novel electron devices and circuit applications as demonstrated for conventional Si-wafers.[29] Utilizing different crystallographic orientations (pFETs on (110) and nFETs on (100)), the drain current in a pFET is shown to be equal to that in an nFET. Howbeit, for the metallic 1T′ phase of MoS_2, we probe into the orientation dependent transport considering the armchair (AA) and zigzag (ZZ) directions. The results obtained using the NEGF-DFT combination reveal that in near-equilibrium, electrical transport in the ZZ_1T′ MoS_2 is almost 3 times greater than that in the AA_1T′ MoS_2. In addition, for the first time (to the best of our knowledge), we conceive atomistic models of the edge contact geometries using monolayer 1T′ MoS_2 and conduct a detailed analysis depicting the charge carrier transport in different metal–1T′ MoS_2 interfaces. We further emphasize the atomic details of the edge contact geometries, considering the regions closer to the interfaces and delineate the electron difference density plots. Next, utilizing the zero bias transmission spectra, we determine the resistance offered by the individual metal–1T′ MoS_2 edge contacts and show that the conductance of the ZZ_1T′ MoS_2 still remains larger (compared to that of the AA_1T′ MoS_2), even after interfacing with metals (*i.e.*, gold and palladium).

2 Methodology and computational details

In order to conduct the first-principles based density functional theory calculations we use the software package Atomistix Tool Kit (ATK).[30] The electronic-structure calculations and geometry optimizations are performed using the generalized gradient approximation (GGA) exchange correlation in conjunction with the Perdew–Burke–Ernzerhof (PBE) functional.[31] It is worth mentioning that in ATK, the accuracy of the computation of electronic properties for any closed/open system basically depends on the quality of the pseudopotentials and the basis sets. Moreover, LCAO (linear combination of atomic orbitals)-based numerical basis sets are utilized here to conduct transport calculations. Thus we had to perform due diligence in selecting a robust pseudopotential-basis set combination which provides results with good accuracy (at the cost of a reasonable computational load).[22,30] We utilize the OPENMX (Open source package for Material eXplorer) code as the norm-conserving pseudopotentials;[32,33] whereas the basis set for "S", "Mo", "Au" and "Pd" are adopted as s2p2d1, s3p2d1, s2p2d1 and s2p2d1 respectively. We further employ Grimme's dispersion correction (DFTD2) in order to apprehend the van der Waals (vdW) interactions.[34] Nonetheless, we set the *k*-points in the Monkhorst–Pack grid as $1 \times 9 \times 9$ (in *X*, *Y* and *Z* directions) for calculating the electronic-structures of the 1T′ supercells (with a density mesh cut off value of 90 Hartree). However, to conduct electrical transport calculations employing the NEGF-DFT combination, we select $1 \times 9 \times 99$ *k*-points in the Monkhorst–Pack grid. In order to solve the Poisson's equation, we assign periodic boundary conditions in the *X*–*Y* directions and Dirichlet boundary conditions in the transport direction (*i.e.*, the *Z* direction).

3 Results and discussion

3.1 Orientation dependent electronic-structures

The optimized unit cell of 1T′ MoS_2 (with lattice constants $a \simeq 3.18$ Å, $b \simeq 5.75$ Å and $c \simeq 18$ Å) is shown in Fig. 1(a). Fig. 1(b) delineates the band structure of the 1T′ unit cell (this is consistent with the previously reported results of ref. 22 and 25). Further, a study on the dynamical stability of the 1T′ phase can be seen in ref. 22. Fig. 2(a) and (b) illustrate the 1T′ MoS_2 flakes which are periodic in the *Y*–*Z* plane. Before investigating the details of the charge carrier transport in AA_1T′ and ZZ_1T′ monolayer MoS_2, we first compare their electronic-structures. Similar to the diamond shaped chains in ReS_2, here also we find a clusterization of the "Mo" atoms. In the case of the AA_1T′ flake, such zigzag-chain clusterization of "Mo" atoms is oriented along the *Y* axis (Fig. 2(c)). However, as shown in Fig. 2(d), for ZZ_1T′ they are arranged in parallel to the direction of transport.

It is important to realize here, that the electronic-structure of MoS_2 predominantly depends on the contributions of the "Mo" atoms (more specifically on the filling of their d-orbitals).[35] Hence, it can be assumed that the clusterization of transition

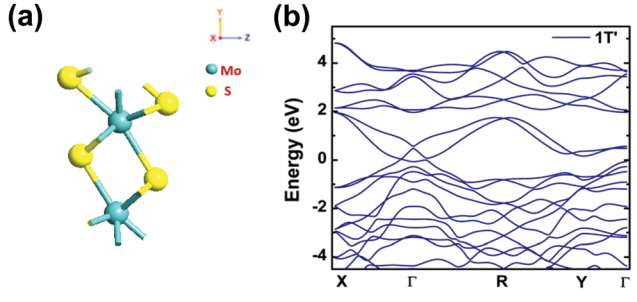

Fig. 1 (a) Unit cell of 1T′ MoS_2, and (b) its band structure.

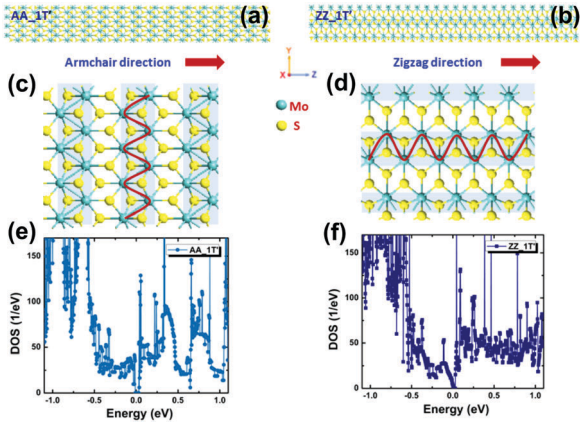

Fig. 2 (a) AA_1T′ and (b) ZZ_1T′ monolayer MoS_2 flakes. For the AA_1T′ sheet, the *Y*–*Z* dimensions are 12.72 Å and ∼9 nm, respectively, whereas the same for the ZZ_1T′ sheet are 11.50 Å and ∼9 nm. Zigzag-chain clusterization of "Mo" atoms for the (c) AA_1T′ MoS_2 and (d) ZZ_1T′ MoS_2 flakes. Density of states diagrams obtained for the AA_1T′ and ZZ_1T′ structures are illustrated in (e) and (f) respectively.

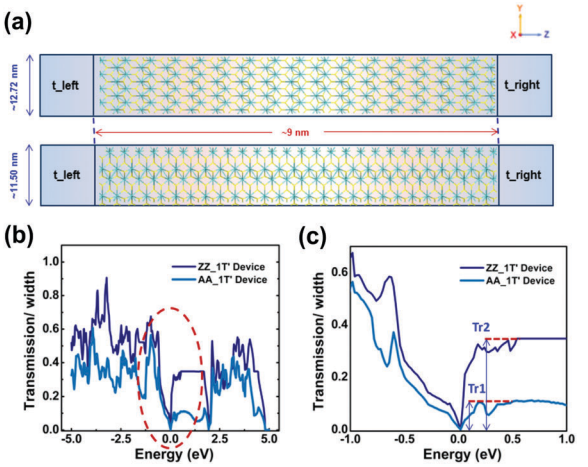

Fig. 3 (a) Two port device structures with AA_1T′ and ZZ_1T′ channels. For the AA_1T′ device, the lengths of the electrodes (t_{left} and t_{right}) are 11.50 Å. For the ZZ_1T′ device, t_{left} and t_{right} are 9.54 Å. (b) Transmission/width of both the devices, obtained for the energy range of (b) −5.0 eV to 5.0 eV and (c) −1.0 eV to 1.0 eV. Moreover, zero energy is represented as the position of the Fermi level.

metal atoms (due to structural distortion) along the axis parallel to the transport direction will largely assist the flow of charge carriers. Perhaps, this gives rise to an increase in the conductance for the ZZ_1T′ structure (which we have elaborately discussed in the following subsection). Moreover, probing into the density of states (DOS) diagrams (Fig. 2(e) and (f)), a very small fundamental gap of ∼0.044 eV (near the energy zero level) is observed for the monolayer 1T′ flake, when it is oriented in the armchair direction. This value of fundamental gap is consistent with the DFT-PBE results, as reported in ref. 25. However, for the ZZ_1T′ MoS_2, we find no such fundamental gap around zero energy (Fermi level).

3.2 Anisotropic transport in 1T′ monolayer MoS_2

Continuing the aforementioned investigation, we further obtain the transmission spectra of the 1T′ MoS_2 sheet oriented in the armchair and zigzag directions. For the purpose of conducting transport studies, we opt for the two port device structures as illustrated in Fig. 3(a). The length of the channel region of those two devices is the same (∼9 nm); whereas the width of the AA_1T′ device is ∼12.72 Å and the same for the ZZ_1T′ device is ∼11.50 Å. Along the perpendicular direction to the *Y*–*Z* plane (*i.e.*, the *X* axis) we incorporate sufficient vacuum in order to avoid any spurious interaction between periodic images.

Fig. 3(b) shows the per width transmission spectra (up spin) of the AA_1T′ and ZZ_1T′ devices. Further, the zoomed-in part shown in Fig. 3(c) compares the transmission/width of both the devices for the energy range of −1.0 eV to 1.0 eV. As the widths of the two port device structures are slightly different, we plot transmission/width instead of transmission, in order to make a fair comparison. It is important to note that we have opted for the spin unpolarized calculations in this study, owing to the fact that there are no significant effects of spin polarization on the transmission spectra. Therefore, the up and down spin components could be considered to be identical. Besides, any effect of spin–orbit coupling (SOC) has not been assessed in the present work.

In the framework of NEGF, electronic transmission through a channel can be computed as,

$$T_e(E) = \mathrm{Tr}[\Gamma_l(E)\, G(E)\, \Gamma_r(E)\, G^{\dagger}(E)], \quad (1)$$

where the key quantities *e.g.*, the retarded Green's function and the advanced Green's function are denoted as $G(E) = [EI - H' - \Sigma_l(E) - \Sigma_r(E)]^{-1}$ and $G^{\dagger}(E)$ respectively.[36,37] H' represents the Hamiltonian of the channel, whereas I denotes an identity matrix. The broadening matrices (formed by setting up the self energy matrices Σ_l and Σ_r) for the left and the right electrodes are described as $\Gamma_{l,r}(E) = i[\Sigma_{l,r} - \Sigma_{l,r}^{\dagger}]$.[3,37] Considering the entire energy range of −5.0 eV to 5.0 eV, we find better transmission in the case of the ZZ_1T′ device, compared to that in the AA_1T′ device (Fig. 3(b)). However, for the calculation of near-equilibrium electrical parameters, the transmission states closer to the Fermi energy (E_F) are important. In order to get a better understanding of the picture, we label the near energy zero transmission/width of the AA_1T′ and ZZ_1T′ devices as Tr1 and Tr2 respectively (Fig. 3(c)). For an energy value of 0.2 eV, Tr2 is calculated as ∼0.314, whereas the Tr1 is ∼0.105 only. Similarly, for the energy value of 0.5 eV, Tr2 and Tr1 are obtained as ∼0.3128 and ∼0.108. Thus, it can be inferred that in near-equilibrium, the electrical transmission in the ZZ_1T′ device is significantly (almost 3 times) larger than that in the AA_1T′ device.

Fig. 4 illustrates the energy-position resolved local density of states (LDOS) diagrams for AA_1T′ and ZZ_1T′ devices. The *Z*-distances denote the channel regions of the two port devices, in real space. The dark and light stripes perpendicular (Fig. 4(a)) and parallel (Fig. 4(b)) to the transport direction (*Z*-axis) originate from the clusterization of "Mo" atoms as discussed qualitatively in Fig. 2(c) and (d). We further probe this clusterization effect on transport by analysing the isosurface plots of valence electron density, obtained for AA_1T′ and ZZ_1T′

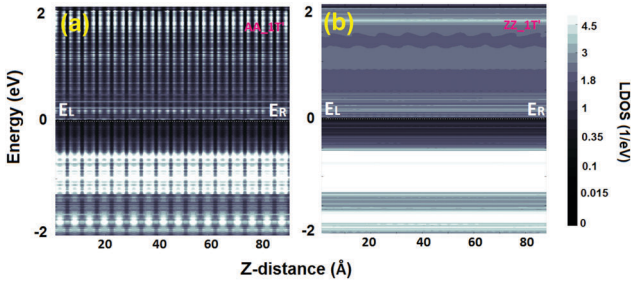

Fig. 4 Energy-position resolved LDOS diagrams for the (a) AA_1T′ and (b) ZZ_1T′ devices, plotted considering the energy range of −2.0 eV to 2.0 eV. The maximum and minimum values of the device density of states (in 1 eV^{-1}) are as depicted in the colour bar. E_L and E_R are the Fermi levels of the left and the right electrodes respectively.

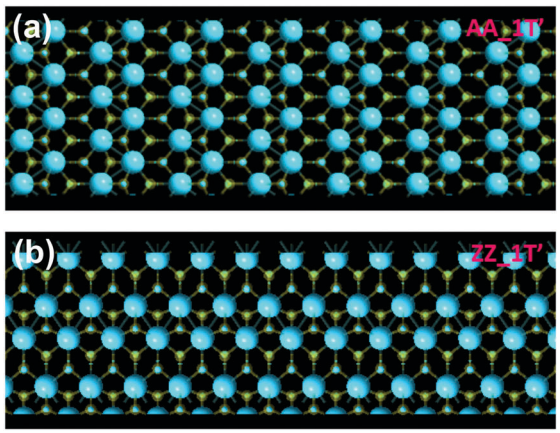

Fig. 5 Isosurface plots depicting the valence electrons around "Mo" atoms, for the (a) AA_1T′ and the (b) ZZ_1T′ devices.

devices (shown in Fig. 5). The minimum and the maximum values of valence electron density for the AA_1T′ device are 0 and 7.9 $Å^{-3}$, whereas the same for the ZZ_1T′ device are computed as 0 and 6.4 $Å^{-3}$ respectively. Comparing the surface plots (drawn with the isovalue of 1.2), we observe that the valence electrons around "Mo" atoms of the ZZ_1T′ device are forming a distribution pattern along the transport direction (*Z*-axis), which is not the case in the AA_1T′ device. This observation is consistent with the LDOS characteristics as depicted in Fig. 4.

Next, we delve into a quantitative analysis by computing the electrical conductance values of the AA_1T′ and ZZ_1T′ devices. For the purpose of deriving conductance values, we utilize the zero bias transmission spectra of both the devices. We evaluate the electrical conductance due to the charge carriers (∼300 K) using the following expression:[37–39]

$$G_e(\mu) = \frac{2q^2}{h}\int_{-\infty}^{+\infty} T_e(E)\left(\frac{-\partial f(\mu,E)}{\partial E}\right)dE. \quad (2)$$

Under the linear response approximation, the above equation can be modified as,[40]

$$G_e(\mu) = q^2 \times L_{f,0}, \quad (3)$$

where the general form of the function $L_{f,n}(\mu)$ is[3,40]

$$L_{f,n}(\mu) = \frac{2}{h} \times \int_{-\infty}^{+\infty} T_e(E)(E-\mu)^n\left(\frac{-\partial f(\mu,E)}{\partial E}\right)dE.$$

We compute the conductance values for the AA_1T′ and ZZ_1T′ devices as 2.275×10^{-5} S and 6.274×10^{-5} S respectively. Thus, for the ZZ_1T′ device, almost a three times improvement in the conductance is evident. Moreover, it is important to notice that the results derived from transport studies are consistent with the electronic-structure calculations described in the previous subsection.

3.3 Metal–1T′ MoS_2 edge contact geometries

3.3.1 Overview of edge contacts. To model the edge contacts with metal surfaces we take the AA_1T′ and the ZZ_1T′ supercells (of Fig. 2) and align those with gold (Au) and palladium (Pd) in the *X*–*Y* plane. As discussed earlier, the major challenge in designing ultrathin transistors with monolayer layer MoS_2 lies in forming the low resistance source/drain contacts. So far, several studies have been reported in the literature delineating the formation of top metal contacts with single layer MoS_2.[16,41–43] MoS_2 is physisorbed on Au(111) and binds with the metal surface at a larger equilibrium distance compared to that on the Pd(111) surface.[16,41] Unfortunately, most of those van der Waals interfaces end up with higher contact resistances, owing to the Schottky barrier limited carrier injection.[41,43] On the other hand, considering the edge contacted metal–MoS_2 hetero-structures, strong orbital overlapping is expected near the interfaces. Smaller physical separations among the metal surface-atoms and the "Mo/S" atoms tend to form covalent bonds.[41,44] Strong orbital overlaps, low tunnel barriers, *etc.* make it favourable for the edge contacts to inject a larger amount of carriers, and thus lowering the contact resistance values.[41,44]

A study on such edge contacted metal–MoS_2 structures can be found in ref. 17, where Liu *et al.* employed DFT simulations to determine the role of the Pd(111)–MoS_2 interface in tuning both piezoelectric and piezotronic effects. Implementation of such contact geometries has also been reported for the other low-dimensional materials like carbon nanotubes (CNTs) and graphene. For example, in ref. 45, Matsuda *et al.* have shown substantial decrease in the contact resistances of the end-contacted metal–graphene and metal–CNT interfaces, using *ab initio* QM (quantum mechanical) calculations.

However, looking into the aspects of the fabrication process, it is quite a difficult task to controllably obtain such metal edge contacts with atomically thin layered materials. In order to design high quality electrical contacts for two dimensional (2D) materials, Wang *et al.* reported a geometry of graphene hetero-structure, where they successfully metallized the one dimensional edge of a 2D sheet.[46] Using electron beam evaporation, they contacted the graphene edge with the metal lead having a typical combination of 1 nm Cr/15 nm Pd/60 nm Au. Nonetheless, they have also confirmed the formation of one dimensional edge contact, with the help of high resolution STEM (scanning transmission electron microscope) imaging and magnified

EELS (electron energy loss spectroscopy) mapping.[46] Apart from that, Ye *et al.* recently demonstrated a similar approach to pattern the edge contact for monolayer TMD *e.g.*, WS_2.[18] For the purpose of forming ohmic contact, they have utilized the technique of electron beam lithography and designed In/Au (10/80 nm) electrodes.[18]

Here, it is worth mentioning that the edges of free-standing monolayer MoS_2 also play an important role in determining the electronic properties. In this context, we may look into the density functional theory calculations of ref. 47, where Bollinger *et al.* confirmed the presence of localized metallic states at the edges. They further modeled the edges by forming a stripe, where the "S" and the "Mo" terminated edges are $(\bar{1}010)$ and $(10\bar{1}0)$ respectively. However, considering the calculated energetics, they have advocated for the "Mo" edge with adsorbed "S" dimers.[47] Nevertheless, with the help of an atom resolved STM image, Helveg *et al.* also revealed that the stable triangular morphology of monolayer MoS_2 clusters (under sulfiding conditions) could have "S" edge atoms which are out of registry with those in the basal plane.[48] Owing to these experimental observations for the semiconducting phase, in this study, we preferred the "S"-ending edge of the AA_1T′ flake (where "Mo" atoms are terminated with "S" atoms, forming "S" dimers). Furthermore, to contact the ZZ_1T′ sheet with metal, we have opted for the edge where S–Mo–S line up along the *Y*-direction.

3.3.2 Atomistic modeling of edge contact geometries. In order to design the metal–1T′ MoS_2 edge contact geometries, we take (111) surface cleaved FCC-Au (of lattice constant 4.07 Å) and FCC-Pd (lattice constant 3.89 Å). For both Au(111) and Pd(111), we take 6 layers of metal which could be sufficient for screening the effect of any surface related phenomenon. Moreover, we try to find a suitable interface geometry where both strain mismatch as well as cell-size are optimum. While the AA_1T′ flake is interfaced with Au(111) and Pd(111) in the *X*–*Y* plane, the mean absolute strain values on metal surfaces are restricted to ∼0.76% and ∼0.57% respectively. For the ZZ_1T′ flake, those values are ∼3.17% only. Next we optimize the metal–1T′ MoS_2 edge contact geometries, utilizing the LBFGS (Limited-memory Broyden Fletcher Goldfarb Shanno) algorithm (with a maximum stress tolerance value of 0.05 eV $Å^{-3}$, and force on each atom smaller than 0.2 eV $Å^{-1}$). For geometry optimization also, we use the OPENMX norm-conserving pseudopotentials,[32,33] along with the basis sets (for "S", "Mo", "Au" and "Pd") as defined in the previous section. However, it is important to note that the outermost layers of both Au(111) and Pd(111) (along the *Z* plane) are constrained, in order to use those layers as electrode extensions.

Fig. 6(a) and (b) illustrate the optimized geometries of Au_AA_1T′ and Au_ZZ_1T′ devices (in the *Y*–*Z* plane), whereas the side-view (*X*–*Z* plane) of those devices can be seen in Fig. 6(c) and (d). Similarly, Fig. 7(a) and (b) depict the relaxed geometries of Pd_AA_1T′ and Pd_ZZ_1T′ devices in the *Y*–*Z* plane (and, the side-views (*X*–*Z* plane) are shown in Fig. 7(c) and (d) respectively).

We further emphasize the atomic details of the edge contact geometries, considering the regions closer to the interfaces. We calculate interface distances among the 1T′ MoS_2 flakes and

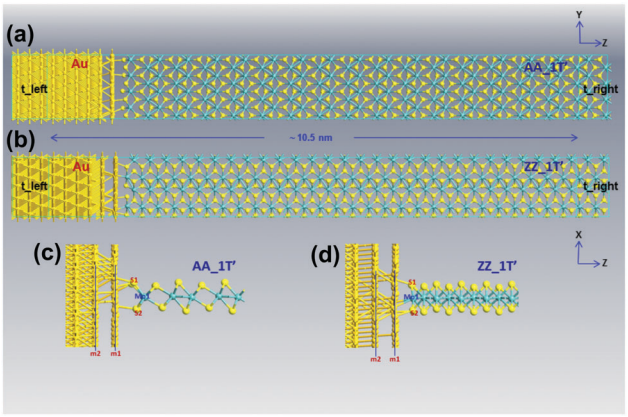

Fig. 6 Optimized geometries of (a) Au_AA_1T′ and (b) Au_ZZ_1T′ devices. For the Au_AA_1T′ device, the lengths of the electrodes (t_{left} and t_{right}) are 7.06 Å and 5.75 Å respectively. For the Au_ZZ_1T′ device, t_{left} and t_{right} are 7.06 Å and 6.36 Å respectively. Besides, the *X*–*Z* plane views of those devices are shown in (c) and (d).

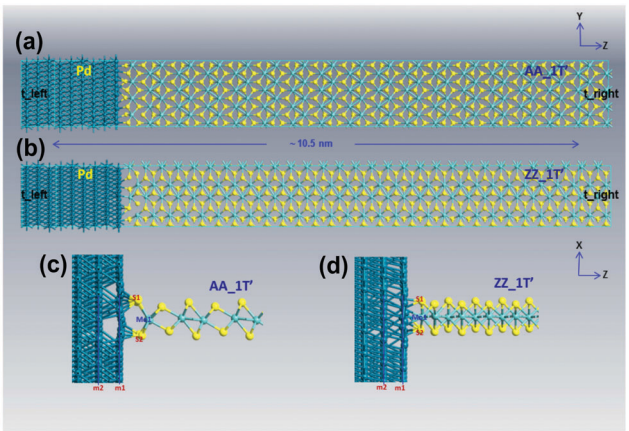

Fig. 7 Optimized geometries of (a) Pd_AA_1T′ and (b) Pd_ZZ_1T′ devices. For the Pd_AA_1T′ device, the lengths of the electrodes (t_{left} and t_{right}) are 6.73 Å and 5.75 Å respectively. For the Pd_ZZ_1T′ device, t_{left} and t_{right} are 6.73 Å and 6.36 Å respectively. Moreover, the side-views (*X*–*Z* plane) of those devices are illustrated in (c) and (d).

first two layers (m1 and m2) of the individual metals. As delineated in the *X*–*Z* view of Fig. 6(c), (d) and 7(c), (d), for each of the optimized edge contact geometries, we opt for two (upper and lower) "S" atoms and a "Mo" atom (near the interface) and mark those as S1, S2 and Mo1 respectively. Nonetheless, the computed distances (considering *Z* co-ordinates) among the highlighted atoms and metal layers are listed in Table 1. From Table 1, we find that the Mo1 atoms for both Au_ZZ_1T′ and Pd_ZZ_1T′ structures are much closer to the metal surface atoms, ensuring strong orbital overlapping in metal–ZZ_1T′ devices (compared to that in metal–AA_1T′ devices).

3.4 Charge carrier transport in metal–1T′ MoS_2 interfaces

Taking the geometries of Fig. 6 and 7 into consideration, in this subsection we discuss the details of charge carrier transport in different metal–1T' MoS_2 interfaces. Fig. 8 and 9, illustrate the

Table 1 Details of interfaces, considering the optimized metal–1T′ MoS_2 edge contact geometries

	Au		Pd	
Z-Distance (Å)	AA_1T′	ZZ_1T′	AA_1T′	ZZ_1T′
d1(S1-m1)	2.35	2.16	1.85	2.09
d2(Mo1-m1)	3.7	2.36	3.04	2.09
d3(S2-m1)	2.67	2.28	2.3	1.94
d4(S1-m2)	4.8	4.63	4.3	4.54
d5(Mo1-m2)	6.16	4.86	5.52	4.56
d6(S2-m2)	5.13	4.79	4.74	4.4

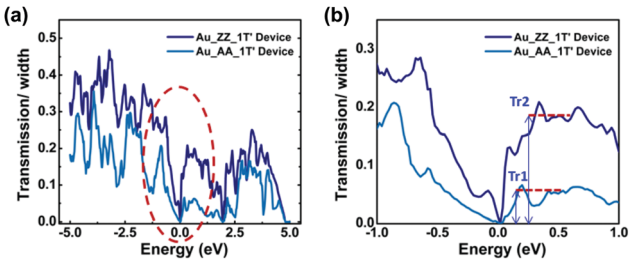

Fig. 8 Transmission/width diagrams of the Au_AA_1T′ and Au_ZZ_1T′ devices, shown for the energy range of (a) −5.0 eV to 5.0 eV and (b) −1.0 eV to 1.0 eV.

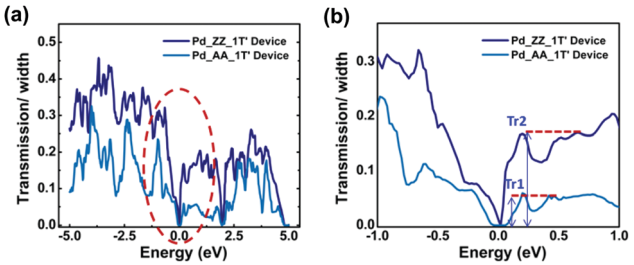

Fig. 9 Transmission/width diagrams of the Pd_AA_1T′ and Pd_ZZ_1T′ devices, shown for the energy range of (a) −5.0 eV to 5.0 eV and (b) −1.0 eV to 1.0 eV.

transmission/width plots (considering the up spin components) of the two port devices. Even after interfacing with metals, we observe that the ZZ_1T′ MoS_2 is more conducive to the charge carrier transport. For the entire energy range of −5.0 eV to 5.0 eV, we find better transmission in the Au_ZZ_1T′ device compared to that in the Au_AA_1T′ device. For the energy value of 0.2 eV, Tr2 and Tr1 are calculated as ∼0.1502 and ∼0.0655 respectively. Besides, the values of Tr2 and Tr1 are obtained as ∼0.1846 and ∼0.0509 respectively, when we shift to a higher energy point, *i.e.*, 0.5 eV. Similarly, inspecting the transmission/width plots of the Pd_AA_1T′ and Pd_ZZ_1T′ devices, we compute the Tr2 and Tr1 values as 0.1675 and 0.0586 for the energy value of 0.2 eV, and 0.1591 and 0.0466 for the energy value of 0.5 eV. Therefore, in near-equilibrium, we notice that the charge carrier transport in metal–ZZ_1T′ devices is almost 2.5 to 3.5 times larger than that in metal–AA_1T′ devices.

Nonetheless, looking at the zoomed-in transmission/width plots of Fig. 8(b) and 9(b), it can be seen that the fundamental gap of the AA_1T′ flake is still evident (near the zero energy) for

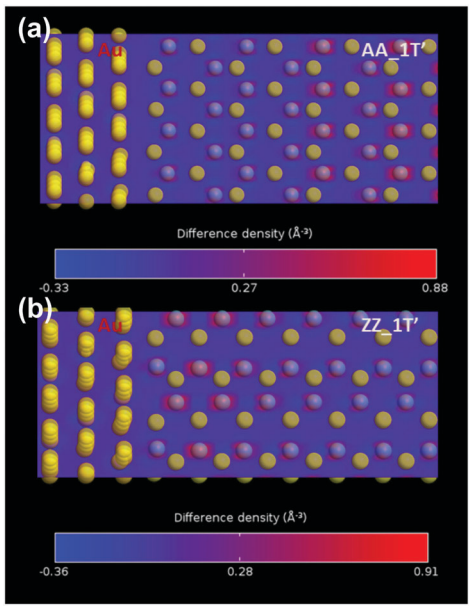

Fig. 10 Cut plane diagrams depicting electron difference density (EDD) in (a) Au_AA_1T′ and (b) Au_ZZ_1T′ interfaces.

both the metal–AA_1T′ interfaces. Interestingly, this gap is even larger (∼−0.04 to ∼+0.06 eV around the E_F) in the case of a Pd_AA_1T′ device. To gain some more insight into the transparency of metal–1T′ MoS_2 interfaces to the charge carrier transport, we next emphasize the electron difference density (EDD) plots, as delineated in Fig. 10 and 11.

In order to illustrate the charge re-distribution, we have focused on the interfacing regions of the different edge contact geometries. A negative value of EDD essentially indicates charge depletion, whereas any positive value implies the accumulation of charge. As shown in the cut plane diagrams (Fig. 10), for Au_AA_1T′

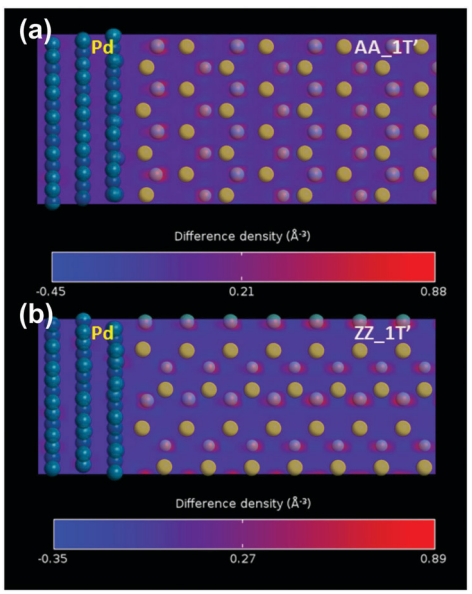

Fig. 11 Cut plane views portraying EDD in (a) Pd_AA_1T′ and (b) Pd_ZZ_1T′ interfaces.

Table 2 Comparison of the resistance values

Device structures	R (Ω μm)
AA_1T′	55.9
Au_AA_1T′	293
Pd_AA_1T′	641
ZZ_1T′	18.3
Au_ZZ_1T′	37.08
Pd_ZZ_1T′	38.6

and Au_ZZ_1T' devices, the minimum and the maximum values of EDD are −0.33 and 0.88 $Å^{-3}$ and −0.36 and 0.91 $Å^{-3}$ respectively. Thus, the corresponding average values are ∼0.27 and ∼0.28 $Å^{-3}$, interpreting more charge distribution in the case of the Au_ZZ_1T′ device. Similarly, for Pd_AA_1T′ and Pd_ZZ_1T′ devices, the minimum and the maximum values of EDD are −0.45 and 0.88 $Å^{-3}$ and −0.35 and 0.89 $Å^{-3}$ respectively (as illustrated in the cut plane diagrams of Fig. 11). However, noting the corresponding average values (which are ∼0.21 and ∼0.27 $Å^{-3}$ respectively), here again we find more charge distribution in the case of the Pd_ZZ_1T′ device. Nevertheless, the trend of these charge distribution oriented results has been more precisely portrayed in the resistance values of the metal–1T′ MoS_2 devices.

Utilizing the zero bias transmission spectra, next we calculate the resistance offered by the individual edge contact geometries. For the metal–1T′ MoS_2 devices (working in a quasi ballistic regime), the resistance values not only include the contributions of the interface/contact regions, but also the parts due to 1T′ MoS_2 flakes. Moreover, for the purpose of comparing the resistances of the metal–1T′ MoS_2 interfaces, we take the normalized (by width) values (denoted as R), instead of the actual ones. We calculate the R for the Au_AA_1T′ and Au_ZZ_1T′ devices as ∼293 Ω μm and ∼37.08 Ω μm respectively. On the other hand, for Pd_AA_1T′ and Pd_ZZ_1T′ devices, the respective values of R have been computed as ∼641 Ω μm and ∼38.6 Ω μm. Therefore, we find a significant improvement in the conductance for the metal–ZZ_1T′ edge contact geometry, irrespective of the choice of metal.

As illustrated in Table 2, the interfaces with Au electrodes offer lesser resistances, compared to those with Pd electrodes. Similar trends of measured contact resistance values can be found in experiments too.[13] Thus, the analyses presented in this study confirm that the formation of edge contacts could be a viable solution to achieve ultra-low resistance source/drain contacts, for the metallic–semiconducting–metallic hetero-phase MoS_2 channels. It is important to realize here that shorter bonding distances among the surface metal atoms and edge Mo/S atoms, and consequently stronger orbital overlapping are the key advantages, of such edge contact geometries over the vdW interfaces.[49] In particular, the absence of any significant effective-barrier at the interfacing regions makes such metal–1T′ MoS_2 devices extremely fruitful.

4 Conclusion

In summary, we have presented a NEGF-DFT study to reveal strong anisotropic conductance of the 1T′ phase of MoS_2. Due to the clusterization of "Mo" atoms along the axis parallel to the transport direction, we find that there is a significant improvement (almost three times) in conductance for the ZZ_1T′ device. Next, to investigate the orientation dependent charge carrier transport in the metal (Au and Pd) interfaces of 1T′ MoS_2, we design the atomistic models of the edge contact geometries. For such metal–1T′ MoS_2 interfaces, strong orbital overlapping plays the pivotal role in attaining ultra-low resistance values. Moreover, our calculations show that the metal–zigzag 1T′ MoS_2 interfaces provide best case results, irrespective of the choice of metal. The values of resistance offered by the Au_ZZ_1T′ and the Pd_ZZ_1T′ devices are ∼37.08 Ω μm and 38.6 Ω μm, respectively, which are extremely promising.

Acknowledgements

This work was supported by the Science and Engineering Research Board (SERB), Department of Science and Technology (DST), Government of India, under Grant No. SB/S3/EECE/0209/2015. The valuable discussions with Dr. Yung-Chang Lin and Dr. Kazu Suenaga of the National Institute of Advanced Industrial Science and Technology, Japan, are gratefully acknowledged. D. S. and S. M. also acknowledge the useful discussions with Dr. Manish Chhowalla of Rutgers University, New Jersey, USA. The authors would like to thank Dr. Kurt Stokbro, Dr. Petr Khomyakov, Dr. Jess Wellendorff, Dr. Daniele Stradi and Dr. Umberto Martinez Pozzoni of QuantumWise A/S Copenhagen, Denmark, for the technical discussions.

References

1 S. Das, J. A. Robinson, M. Dubey, H. Terrones and M. Terrones, Beyond Graphene: Progress in Novel Two-Dimensional Materials and van der Waals Solids, *Annu. Rev. Mater. Res.*, 2015, **45**, 1–27.
2 K. F. Mak and J. Shan, Photonics and optoelectronics of 2D semiconductor transition metal dichalcogenides, *Nat. Photonics*, 2016, **10**, 216–226, DOI: 10.1038/NPHOTON.2015.282.
3 D. Saha and S. Mahapatra, Theoretical insights on the electro-thermal transport properties of monolayer MoS_2 with line defects, *J. Appl. Phys.*, 2016, **119**, 134304, DOI: http://dx.doi.org/10.1063/1.4945582.
4 D.-H. Lien, J. S. Kang, M. Amani, K. Chen, M. Tosun, H.-P. Wang, T. Roy, M. S. Eggleston, M. C. Wu, M. Dubey, S.-C. Lee, J.-H. He and A. Javey, Engineering Light Outcoupling in 2D Materials, *Nano Lett.*, 2015, **15**, 1356–1361, DOI: 10.1021/nl504632u.
5 S. Bertolazzi, J. Brivio and A. Kis, Stretching and Breaking of Ultrathin MoS_2, *ACS Nano*, 2011, **5**(12), 9703–9709.
6 T. Stephenson, Z. Li, B. Olsen and D. Mitlin, Lithium ion battery applications of molybdenum disulfide (MoS_2) nanocomposites, *Energy Environ. Sci.*, 2014, **7**, 209–231.
7 C.-H. Lee, *et al.*, Atomically thin pn junctions with van der Waals heterointerfaces, *Nat. Nanotechnol.*, 2014, **9**, 676–681.
8 M. M. Furchi, A. Pospischil, F. Libisch, J. Burgdörfer and T. Mueller, Photovoltaic Effect in an Electrically Tunable van der Waals Heterojunction, *Nano Lett.*, 2014, **14**, 4785–4791.

9 J. Pak, J. Jang, K. Cho, T.-Y. Kim, J.-K. Kim, Y. Song, W.-K. Hong, M. Min, H. Lee and T. Lee, Enhancement of photodetection characteristics of MoS_2 field effect transistors using surface treatment with copper phthalocyanine, *Nanoscale*, 2015, **7**, 18780–18788.

10 B. Radisavljevic, A. Radenovic, J. Brivio, V. Giacometti and A. Kis, Single-layer MoS_2 transistors, *Nat. Nanotechnol.*, 2011, **6**, 147–150.

11 K. Alam and R. Lake, Monolayer MoS_2 Transistors Beyond the Technology Road Map, *IEEE Trans. Electron Devices*, 2012, **59**(12), 3250–3254.

12 International Technology Roadmap for Semiconductors (ITRS) 2013, Available at http://www.itrs2.net/2013-itrs.html.

13 R. Kappera, D. Voiry, S. E. Yalcin, B. Branch, G. Gupta, A. D. Mohite and M. Chhowalla, Phase-engineered low-resistance contacts for ultrathin MoS_2 transistors, *Nat. Mater.*, 2014, **13**, 1128–1134, DOI: 10.1038/NMAT4080.

14 Z. Ni, M. Ye, J. Ma, Y. Wang, R. Quhe, J. Zheng, L. Dai, D. Yu, J. Shi, J. Yang, S. Watanabe and J. Lu, Performance Upper Limit of sub-10 nm Monolayer MoS_2 Transistors, *Adv. Electron. Mater.*, 2016, 1600191, DOI: 10.1002/aelm.201600191.

15 F. Ahmed, M. S. Choi, X. Liu and W. J. Yoo, Carrier transport at the metal–MoS_2 interface, *Nanoscale*, 2015, **7**, 9222–9228, DOI: 10.1039/c5nr01044f.

16 M. Farmanbar and G. Brocks, First-principles study of van der Waals interactions and lattice mismatch at MoS_2/metal interfaces, *Phys. Rev. B*, 2016, **93**, 085304.

17 W. Liu, A. Zhang, Y. Zhang and Z. L. Wang, Density functional studies on edge-contacted single-layer MoS_2 piezotronic transistors, *Appl. Phys. Lett.*, 2015, **107**, 083105.

18 Y. Ye, J. Xiao, H. Wang, Z. Ye, H. Zhu, M. Zhao, Y. Wang, J. Zhao, X. Yin and X. Zhang, Electrical generation and control of the valley carriers in a monolayer transition metal dichalcogenide, *Nat. Nanotechnol.*, 2016, **11**, 598–602, DOI: 10.1038/nnano.2016.49.

19 Y.-C. Lin, D. O. Dumcenco, Y.-S. Huang and K. Suenaga, Atomic mechanism of the semiconducting-to-metallic phase transition in single-layered MoS_2, *Nat. Nanotechnol.*, 2014, **9**, 391–396, DOI: 10.1038/NNANO.2014.64.

20 Y. Katagiri, T. Nakamura, A. Ishii, C. Ohata, M. Hasegawa, S. Katsumoto, T. Cusati, A. Fortunelli, G. Iannaccone, G. Fiori, S. Roche and J. Haruyama, Gate-Tunable Atomically Thin Lateral MoS_2 Schottky Junction Patterned by Electron Beam, *Nano Lett.*, 2016, **16**, 3788–3794, DOI: 10.1021/acs.nanolett.6b01186.

21 A. Nourbakhsh, A. Zubair, R. N. Sajjad, K. G. Amir Tavakkoli, W. Chen, S. Fang, X. Ling, J. Kong, M. S. Dresselhaus, E. Kaxiras, K. K. Berggren, D. Antoniadis and T. Palacios, MoS_2 Field-Effect Transistor with Sub-10 nm Channel Length, *Nano Lett.*, 2016, **16**, 7798–7806, DOI: 10.1021/acs.nanolett.6b03999.

22 D. Saha and S. Mahapatra, Atomistic modeling of the metallic-to-semiconducting phase boundaries in monolayer MoS_2, *Appl. Phys. Lett.*, 2016, **108**, 253106, DOI: http://dx.doi.org/10.1063/1.4954257.

23 D. Saha and S. Mahapatra, Asymmetric Junctions in Metallic-Semiconducting-Metallic Heterophase MoS_2, *IEEE Trans. Electron Devices*, DOI: 10.1109/TED.2017.2680453.

24 G. Gao, Y. Jiao, F. Ma, Y. Jiao, E. Waclawik and A. Du, Charge Mediated Semiconducting-to-Metallic Phase Transition in Molybdenum Disulphide Monolayer and Hydrogen Evolution Reaction in New 1T′ Phase, *J. Phys. Chem. C*, 2015, **119**, 13124–13128, DOI: 10.1021/acs.jpcc.5b04658.

25 X. Qian, J. Liu, L. Fu and J. Li, Quantum spin Hall effect in two-dimensional transition metal dichalcogenides, *Science*, 2014, **346**(6215), 1344–1347, DOI: 10.1126/science.1256815.

26 D. B. Putungan, S.-H. Lin and J.-L. Kuo, A first-principles examination of conducting monolayer 1T′-MX_2 (M = Mo, W; X = S, Se, Te): promising catalysts for hydrogen evolution reaction and its enhancement by strain, *Phys. Chem. Chem. Phys.*, 2015, **17**, 21702–21708.

27 Y.-C. Lin, H.-P. Komsa, C.-H. Yeh, T. Bjorkman, Z.-Y. Liang, C.-H. Ho, Y.-S. Huang, P.-W. Chiu, A. V. Krasheninnikov and K. Suenaga, Single-Layer ReS_2: Two-Dimensional Semiconductor with Tunable In-Plane Anisotropy, *ACS Nano*, 2015, **9**(11), 11249–11257.

28 F. Liu, Y. Wang, X. Liu, J. Wang and H. Guo, A Theoretical Investigation of Orientation-Dependent Transport in Monolayer MoS_2 Transistors at the Ballistic Limit, *IEEE Electron Device Lett.*, 2015, **36**(10), 1091–1093.

29 M. Yang, *et al.* High Performance CMOS Fabricated on Hybrid Substrate With Different Crystal Orientations, *IEEE International Electron Devices Meeting 2003*, Washington, DC, USA, 2003, pp. 18.7.1–18.7.4.

30 QuantumWise Atomistix ToolKit (ATK) with Virtual NanoLab, Available at http://quantumwise.com/.

31 J. P. Perdew, K. Burke and M. Ernzerhof, Generalized Gradient Approximation Made Simple, *Phys. Rev. Lett.*, 1996, **77**(18), 3865–3868, DOI: https://doi.org/10.1103/PhysRevLett.77.3865.

32 T. Ozaki, Variationally optimized atomic orbitals for large-scale electronic structures, *Phys. Rev. B: Condens. Matter Mater. Phys.*, 2003, **67**, 155108, DOI: doi: 10.1103/PhysRevB.67.155108.

33 T. Ozaki and H. Kino, Numerical atomic basis orbitals from H to Kr, *Phys. Rev. B: Condens. Matter Mater. Phys.*, 2004, **69**, 195113, DOI: 10.1103/PhysRevB.69.195113.

34 S. Grimme, Semiempirical GGA-type density functional constructed with a long-range dispersion correction, *J. Comput. Chem.*, 2006, **27**(15), 1787–1799.

35 M. Chhowalla, H. S. Shin, G. Eda, L.-J. Li, K. P. Loh and H. Zhang, The chemistry of two-dimensional layered transition metal dichalcogenide nanosheets, *Nat. Chem.*, 2013, **5**, 263–275.

36 M. Brandbyge, J.-L. Mozos, P. Ordejón, J. Taylor and K. Stokbro, Density-functional method for nonequilibrium electron transport, *Phys. Rev. B: Condens. Matter Mater. Phys.*, 2002, **65**, 165401, DOI: 10.1103/PhysRevB.65.165401.

37 T. Markussen, A.-P. Jauho and M. Brandbyge, Electron and phonon transport in silicon nanowires: atomistic approach to thermoelectric properties, *Phys. Rev. B: Condens. Matter Mater. Phys.*, 2009, **79**, 035415.

38 M. Büttiker, Y. Imry, R. Landauer and S. Pinhas, Generalized many-channel conductance formula with application to small rings, *Phys. Rev. B: Condens. Matter Mater. Phys.*, 1985, **31**(10), 6207–6215.

39 D. Stradi, U. Martinez, A. Blom, M. Brandbyge and K. Stokbro, General atomistic approach for modeling metal–semiconductor interfaces using density functional theory and nonequilibrium Green's function, *Phys. Rev. B*, 2016, **93**, 155302, DOI: 10.1103/PhysRevB.93.155302.

40 K. Esfarjani, M. Zebarjadi and Y. Kawazoe, Thermoelectric properties of a nanocontact made of two-capped single-wall carbon nanotubes calculated within the tight-binding approximation, *Phys. Rev. B: Condens. Matter Mater. Phys.*, 2006, **73**, 085406.

41 J. Kang, W. Liu, D. Sarkar, D. Jena and K. Banerjee, Computational Study of Metal Contacts to Monolayer Transition-Metal Dichalcogenide Semiconductors, *Phys. Rev. X*, 2014, **4**, 031005.

42 C. D. English, G. Shine, V. E. Dorgan, K. C. Saraswat and E. Pop, Improved Contacts to MoS_2 Transistors by Ultra-High Vacuum Metal Deposition, *Nano Lett.*, 2016, **16**, 3824–3830.

43 C. Gong, L. Colombo, R. M. Wallace and K. Cho, The Unusual Mechanism of Partial Fermi Level Pinning at Metal–MoS_2 Interfaces, *Nano Lett.*, 2014, **14**, 1714–1720.

44 X. Liu, G. Zhang and Y.-W. Zhang, Thermal conduction across the one-dimensional interface between a MoS_2 monolayer and metal electrode, *Nano Res.*, 2016, **9**(8), 2372–2383.

45 Y. Matsuda, W.-Q. Deng and W. A. Goddard, Contact Resistance for "End-Contacted" Metal–Graphene and Metal–Nanotube Interfaces from Quantum Mechanics, *J. Phys. Chem. C*, 2010, **114**, 17845–17850.

46 L. Wang, I. Meric, P. Y. Huang, Q. Gao, Y. Gao, H. Tran, T. Taniguchi, K. Watanabe, L. M. Campos, D. A. Muller, J. Guo, P. Kim, J. Hone, K. L. Shepard and C. R. Dean, One-Dimensional Electrical Contact to a Two-Dimensional Material, *Science*, 2013, **342**(6158), 614–617.

47 M. V. Bollinger, J. V. Lauritsen, K. W. Jacobsen, J. K. Nørskov, S. Helveg and F. Besenbacher, One-Dimensional Metallic Edge States in MoS_2, *Phys. Rev. Lett.*, 2001, **87**(19), 196803.

48 S. Helveg, J. V. Lauritsen, E. Lægsgaard, I. Stensgaard, J. K. Nørskov, B. S. Clausen, H. Topsøe and F. Besenbacher, Atomic-Scale Structure of Single-Layer MoS_2 Nanoclusters, *Phys. Rev. Lett.*, 2000, **84**(5), 951–954.

49 A. Allain, J. Kang, K. Banerjee and A. Kis, Electrical contacts to two-dimensional semiconductors, *Nat. Mater.*, 2015, **14**, 1195–1205.